## PAPER

Check for updates

# Nanoscale carbonaceous materials *via* element hyperaccumulation for electrochemical desalination application

Juan Zhou, Xue-Jing Ma, ⓘ * Ashkar Batol, Huan Gou, Jie Feng, Xia-Yue Yuan, Jun-Hu Liu and Wei-Bin Zhang ⓘ *

Developing renewable green electrode materials with outstanding electrochemical properties is essential for advancing the practical application of flow electrode capacitive deionization (FCDI) technology. This study introduces an innovative green biosorption approach combined with a carbonization technique to fabricate self-doped manganese biomass-derived porous carbon. The resulting composite possesses a high specific surface area of 635.24 $m^2$ $g^{-1}$, which facilitates the exposure of more active adsorption sites and ion transport pathways. Furthermore, the synergistic interaction between the electric double-layer capacitance of biomass-derived porous carbon and the pseudocapacitance of transition metal manganese enables the electrode material to show exceptional electrochemical performance, achieving a specific capacitance of 137.30 F $g^{-1}$ at a current density of 0.25 A $g^{-1}$. When integrated into an FCDI system, the electrode material reaches a high salt adsorption capacity of 459.51 mg $g^{-1}$ and a high average desalination rate of 9.95 mg $g^{-1}$ $h^{-1}$ under identified optimal conditions. Moreover, after extended desalination cycles, the retention rates for both salt adsorption capacity and average desalination rate remain approximately 70%. Notably, this novel approach not only paves the way for designing transition metal-doped biomass-derived porous carbon materials but also contributes to mitigating environmental pollution caused by manganese metals.

## 1. Introduction

The global shortage of freshwater resources has seriously threatened the survival and sustainable development of mankind. Although traditional desalination technologies such as thermal desalination (flash distillation, multi-effect distillation or mechanical distillation compression)[1,2] and membrane desalination (reverse osmosis or electrodialysis)[3,4] have alleviated the pressure on freshwater demand to some extent, they still have problems such as high operating costs, consumption of huge amounts of energy and potential secondary pollution.[5] Therefore, the research and development of seawater desalination technology with excellent desalination performance, significant cost advantages and good environmental compatibility have become a technical bottleneck that needs to be overcome in the current water treatment field.

Capacitive deionization (CDI) technology achieves seawater desalination through electrical energy-driven chemical reactions[6] and has been widely developed because of its advantages of energy saving, environmental protection, flexible scale and no secondary pollution. However, it is found that there is

an obvious bottleneck in the deionization capacity of fixed electrode CDI cells, and the collector size limits the number of active electrodes, which directly affects the overall performance of the system. In addition, the traditional CDI systems face the technical problem of electrode saturation, which often requires intermittent regeneration of electrodes by short circuit or application of a reverse voltage,[7] which increases the complexity of system operation and reduces the efficiency of desalination. To alleviate such a problem, Jeon *et al.*[8] developed the flow electrode capacitive deionization (FCDI) in 2013 with the aim of addressing the limitations of conventional deionization techniques. The technology uses flow electrodes instead of conventional solid electrodes, and the electrode slurry enters the FCDI unit through a serpentine channel in the collector. The intermediate chamber, which treats the brine, is physically separated from the electrode chambers on both sides by an ion exchange membrane. Under the action of an electric field, salt ions in the intermediate chamber migrate directionally to the electrode chamber through the anion exchange membrane and are subsequently adsorbed on the flowing electrode particles, thus effectively reducing the salinity of the effluent solution. After the adsorption process is completed, the electrode can be regenerated by applying a reverse potential. This technological breakthrough solves the key problems of traditional electrodes, such as easy saturation and low regeneration

*College of Materials and Chemistry & Chemical Engineering, Chengdu University of Technology, Chengdu 610059, China. E-mail: maxuejing17@cdut.edu.cn, zhangweibin17@cdut.edu.cn*

efficiency, and provides a new technological path for efficient seawater desalination.[9]

In the field of FCDI, carbon-based materials such as activated carbon (AC), carbon nanotubes, carbon nanofibers and graphene occupy an important position in electrochemistry by virtue of their excellent electrochemical stability, outstanding electrical conductivity and unique structure.[10] However, these materials face a number of challenges in practical applications. Their single structure makes it difficult to achieve satisfactory electrochemical performance, and the pore structure modulation process is complicated and expensive, which seriously restrict the large-scale application of carbon-based materials. In recent years, renewable biomass-derived carbon materials in the field of flow electrode capacitive deionization have been subjected to increasingly in-depth research; their large specific surface areas for ion adsorption provide sufficient active sites, their adjustable pore size structures help achieve selective ion transport, their excellent chemical stability ensures that they withstand long term use in a complex aqueous environment, and this kind of material is inexpensive and easy to process, laying the foundation for large-scale applications.[11] Furthermore, the unique structure and the presence of heteroatoms (N, S, B and P) in biomass resources have also been shown to enhance ion storage performance by improving the wettability and conductivity of materials, and providing additional pseudocapacitance and defective structures.[12–15] Unfortunately, bare biomass-derived porous carbon materials are limited by the double layer capacitance energy storage mechanism, which results in a single process of charge accumulation at the electrode interface, making it impossible to achieve satisfactory specific capacitance performance.[16] A large number of studies have proved that by introducing pseudocapacitors with Faraday reaction or reversible redox properties into porous carbon materials, the synergistic effect of electric double-layer capacitance and pseudocapacitance can be effectively realized, and the specific capacitance performance of the materials can be significantly improved.[17–19]

On the other hand, transition metal oxides (TMO) are pseudocapacitive materials with great development potential. Among them, the typical $MnO_x$ is highly valued in the field of FCDI due to its reversible faradaic reaction, high theoretical specific capacitance, low production cost, wide potential window[20] and wide natural availability. However, despite the good performance of $MnO_x$ electrode materials, their inherent low conductivity severely limits the electron transfer efficiency, and the slow ion diffusion kinetics during charge/discharge cycling further aggravates the degradation of the material properties, which will limit their practical applications in the field of electrochemical energy storage.[21] Therefore, it has been shown that the synergistic effect between the transition metal manganese oxide and porous carbon materials can not only improve the conductivity, but also provide a channel for charge transport, so as to obtain excellent electrochemical properties. Van Lam et al.[22] used a laser scribing technique to convert Mn-based metal–organic frameworks EG-MOF-74(Mn) into pseudocapacitance hybridized $MnO/Mn_7C_3$ materials,

exploiting the synergistic effect generated between $MnO/Mn_7C_3$ nanoparticles and graphitic carbon, resulting in composites that exhibit significant advantages in electrochemical performance, with electrochemical specific capacitances as high as 403 F $g^{-1}$ and excellent cycling stability. Han et al.[23] successfully synthesized hierarchical porous manganese oxide/carbon (MnO/C) microsphere materials using a combination of chemical solution and high-temperature pyrolysis techniques. The material was optimized to exhibit excellent electrochemical properties, with a specific capacitance of 378 F $g^{-1}$ at a 0.1 A $g^{-1}$ current density, and its cycling stability was outstanding, with a capacitance retention of 96.66% after 1000 cycles at a 1 A $g^{-1}$ current density. Li et al.[24] used the KOH activation technique to construct the porous structure, combined with the hydrothermal method to successfully load manganese oxides onto the surface of biomass porous carbon, and prepared the manganese oxide/biomass porous carbon composites. The electrochemical performance test shows that the composite exhibits excellent capacitance characteristics in the three-electrode system, and its specific capacitance value reaches 482 F $g^{-1}$ at a 0.5 A $g^{-1}$ current density. Zhao et al.[25] first carbonized grapefruit peel into biomass carbon, and then prepared sea urchin manganese-like manganese/biomass composites with porosity and high specific surface area (SSA) by hydrothermal reaction with potassium permanganate. The electrochemical specific capacitance of the electrode can be as high as 205.5 F $g^{-1}$ at 0.5 A $g^{-1}$, and it also exhibits good long cycling capability after 4000 charge–discharge cycles. However, although it can be proved that the manganese oxide loading can effectively increase the specific capacitance, there are still some problems, such as low efficiency, irregular structure and uncontrollable loading of manganese oxide on porous carbon materials, which will directly affect the electrochemical properties of the materials.[19,23,24] Therefore, a simple, efficient and green method was found to prepare manganese oxide and biomass-derived carbon composites. Fortunately, the superaccumulation properties of plants can effectively convert manganese ions into organic salts to accumulate in cells, which can subsequently be used to prepare manganese self-doped biomass-derived carbons.[26,27]

At the same time, the demand for manganese continues to rise as a result of rapid economic development, and the problem of water pollution caused by the over-exploitation of manganese ore resources is becoming more and more prominent.[28] Therefore, controlling and mitigating the pollution of heavy metal manganese to water resources has also become an urgent problem to be solved. The results show that the use of phytoremediation in biological methods can not only save costs, but also effectively deal with manganese pollution. Through existing research, it has been proved that leafy herbs are the most heavily enriched and polluted plants with heavy metals,[29,30] while *Epipremnum aureum* (EA) as a typical ornamental plant in hydroponics shows rapid growth and possesses a rich void structure which are of significant advantage in the process of manganese enrichment. This plant can efficiently adsorb manganese ions in the aqueous environment through its rich void network while maintaining the integrity

of the original pore structure. In view of this, we chose EA as a carrier for super-enriched manganese, and used its super-accumulation characteristics to convert manganese ions into organic salts and accumulate them in cells, and then *in situ* doped biomass-derived carbon composites with manganese.

In this work, EA was initially cultured in an aqueous manganese nitrate solution at a concentration of 0.02 M to enrich the manganese elements, and then carbonized to obtain *in situ* manganese-doped porous carbon Mn@EAC. The prepared composites demonstrated a synergistic effect between the electric double-layer capacitance of biochar and the pseudocapacitance of manganese, leading to superior electrochemical performance and long-term desalination cycling stability. This research result not only provides new ideas for the design of transition metal-modified biomass-derived porous carbon materials, but also opens up an innovative way to solve the problem of high value-added utilization of biomass and heavy metal manganese in water pollution.

## 2.  Experimental and characterization

### 2.1.  Biosynthesis and characterization of materials

The schematic diagram of the preparation process of Mn@EAC-*x* (*x* means *x* days) is shown in Fig. 1. EA with a similar growth status was selected for the experiment, and was cultured in a deionized water environment for 10 days before being transferred to 200 mL of manganese nitrate solution with a concentration of 0.02 M for secondary culture. Samples were taken at 10-day intervals, and the stem and leaf parts of the plants were collected, washed several times with deionized water, and then placed in a constant temperature oven at 60 °C for 48 h of drying treatment. Subsequently, the samples were placed in a tube furnace and heated to 500 °C for 1 h of pre-carbonization at a rate of 5 °C min$^{-1}$ under a $N_2$ protective atmosphere, followed by heating to 800 °C for 2 h of final carbonization. The resulting product was washed to neutrality with deionized water and then dried at 60 °C for 24 h to obtain *in situ* manganese-doped biomass-derived carbon (Mn@EAC-*x*).

The manganese content in Mn@EAC-*x* was analyzed using an inductively coupled plasma spectrometer (ICP-OES, Agilent 5110). The crystal structures of active carbon (AC) and Mn@EAC-*x* were determined using an X-ray diffractometer (XRD, Anton Paar XRDynamic500, Austria). The wettability of AC and Mn@EAC-*x* was analyzed by a contact angle test. The morphology and element distribution were studied using a scanning electron microscope (SEM, ZEISS Sigma 360, Germany) and a transmission electron microscope (TEM, JEOL JEM 2100F, Japan) equipped with an energy dispersive spectrometer. The specific surface area and pore size distribution of the material were analyzed using an automatic specific surface area and porosity analyzer (BET, Micromeritics ASAP2460). Raman spectroscopy was performed using a Raman spectrometer (Renishaw inVia, UK) with a laser wavelength of 532 nm.

### 2.2.  Electrochemical measurement and deionization performance

First, the active material Mn@EAC-*x*/AC, the binder polytetrafluoroethylene (PTFE), and the conductive additive graphite powder were weighed at a mass ratio of 8 : 1 : 1, with the active material mass being 8 mg. The mixture was thoroughly ground to homogeneity, and an appropriate amount of *N*-methyl-2-pyrrolidone (NMP) was added dropwise with stirring until a uniform slurry formed. This slurry was then uniformly coated onto a graphite sheet (1 cm × 1 cm) and transferred to a constant temperature oven at 60 °C for overnight drying. After drying, the material was densified using a pressing pressure of 10 MPa to obtain a working electrode with a stable structure. Finally, a three-electrode system was assembled with an Ag/AgCl reference electrode, a Pt counter electrode and a prepared working electrode, and the electrochemical properties (CV, GCD, and EIS) of the electrode materials were tested using a Shanghai Chenhua CHI660E electrochemical workstation. The CV test was conducted at different scan rates between −1 V and 1 V, and the areal specific capacitance ($C_1$, F g$^{-1}$) in the cyclic voltammetry test was calculated according to eqn (1):[31]

$$C_1 = \frac{\int i \, \mathrm{d}v}{2\Delta V m v} \tag{1}$$

where $C_1$ is the areal specific capacitance of the electrode (F g$^{-1}$), $i$ is the applied current (A), $\Delta V$ is the voltage window of the CV curve (V), $m$ is the effective mass of the active material on the electrode sheet (g), and $v$ is the scan rate.



Botanical name: Epipremnum aureum. Source of the Mn$^{2+}$(aq.): 0.02 M aqueous Mn(NO$_3$)$_2$ simulated wastewater.
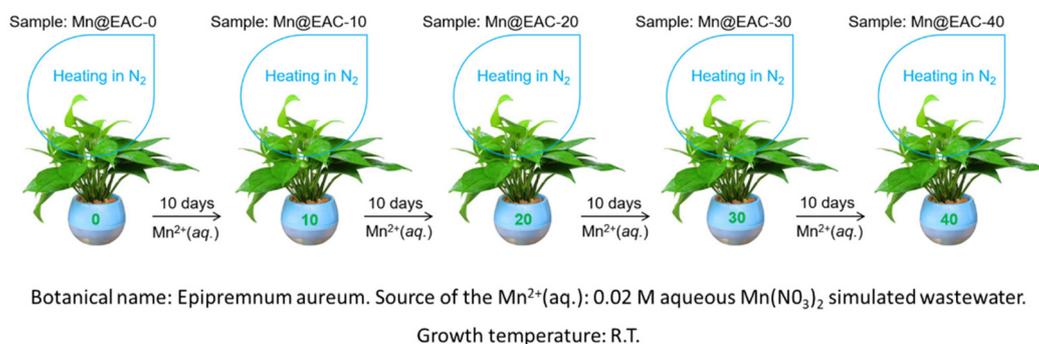
Growth temperature: R.T.

**Fig. 1**  Schematic diagram of the preparation process of Mn@EAC-*x*.

The GCD was tested at different current densities between −1 V and 0 V in terms of voltage. Eqn (2) was used to determine the specific capacitance ($C_2$, F g$^{-1}$) in the charge–discharge test with a constant current:

$$C_2 = \frac{I\Delta t}{m\Delta V} \qquad (2)$$

where $C_2$ is the specific capacitance of the electrode (F g$^{-1}$), $I$ is the current response (A), $\Delta t$ is the discharge time (s), $m$ is the effective mass of the active material on the electrode sheet (g), and $\Delta V$ is the scanning potential range.

The detailed schematic of the working principle of the FCDI system is illustrated in Fig. S1. Firstly, the mobile electrode was dispersed in an aqueous solution of NaCl (500 mg L$^{-1}$, 100 mL), stirred magnetically for 2 h, and the content of the mobile electrode was selected as 60–100 mg, and secondly, the aqueous solution of NaCl of the same concentration was configured as the simulated seawater, and then two peristaltic pumps were used to circulate the mobile electrode and simulated seawater at different operating voltages (0.8–1.3 V) at the same electrode flow rate (15–35 mL min$^{-1}$). Finally, the conductivity change of simulated seawater was monitored and recorded in real time using a conductivity meter (DDSJ-319L, Shanghai Leici). The salt adsorption capacity ($\Gamma$) and average desalination rate ($\varphi$) of the electrode materials can be calculated using eqn (2) and (3), respectively:[32]

$$\Gamma = \frac{(G_0 - G_t)V}{m} \qquad (3)$$

$$\varphi = \frac{(G_0 - G_t)V}{m\Delta t} \qquad (4)$$

where $\Gamma$ is the salt adsorption capacity (mg g$^{-1}$), $\varphi$ is the desalination efficiency (mg g$^{-1}$ h$^{-1}$), $G_0$ and $G_t$ are the initial and final NaCl concentrations (mg L$^{-1}$), $V$ is the total volume of the salt solution (L), $m$ is the effective mass of the active material in the flow electrode (g), and $\Delta t$ is the charging time (h).

## 3. Results and discussion

### 3.1. Microstructures of the materials

The structures of the AC and Mn@EAC-$x$ have been characterized by XRD, as shown in Fig. 2a; all materials exhibited two wide diffraction peaks, corresponding to the (002) and (100) crystal planes of graphitic carbon, respectively, revealing that the prepared Mn@EAC-$x$ has a typical amorphous carbon structure.[33] Fig. 2d shows the Raman tests of AC and Mn@EAC-$x$ materials, and it can be seen that all the samples present characteristic peaks at 1340 cm$^{-1}$ and 1600 cm$^{-1}$, which correspond to the D and G bands of the carbon materials, respectively, where the D band indicates the sp$^3$ hybridized carbon structure or edge defects, and the G band indicates the in-plane vibration modes of the sp$^2$ hybridized carbon atoms.[34] Finally, the graphitization characteristics of the materials were quantitatively evaluated by calculating the intensity ratio of the D to G bands ($I_D/I_G$). The measured $I_D/I_G$

values for AC, Mn@EAC-0, Mn@EAC-30, and Mn@EAC-40 were 0.9818, 0.9972, 0.9954, and 0.9882, respectively. This trend indicates that during the hydroponic process of EA, the absorbed manganese ions functioned as catalysts in the subsequent pyrolysis, facilitating the transformation of amorphous carbon into an ordered graphitic structure and thereby enhancing the graphitization degree of the material. The improved graphitization endows the materials with excellent electrical conductivity, which ensures faster electron transfer and more efficient ion adsorption/desorption kinetics in the FCDI process, ultimately leading to significantly enhanced desalination efficiency of the FCDI system. The amount of manganese doped in the composites was then determined by ICP-OES, and as shown in Fig. 2e, the manganese content in the composites increased with the extension of the incubation time. The manganese content gradually accumulated from 113.57 mg kg$^{-1}$ on day 0 to 609.98 mg kg$^{-1}$ on day 40.

To thoroughly elucidate the regulatory effect of hyperaccumulation on the porous structure of the materials, this study conducted quantitative analysis of the specific surface area and pore size distribution of the Mn@EAC-$x$ series through systematic N$_2$ adsorption–desorption tests (relevant data are detailed in Table S1). As shown in Fig. 2b and S2, the isotherms of all materials exhibit typical type IV characteristics, with distinct hysteresis loops observed in the relative pressure ($P/P_0$) range of 0.4–0.9, indicating the presence of a typical mesoporous structure in the materials.[35] As can be observed, with the extension of manganese hyperaccumulation time, the pore structure of the materials exhibits a significant evolutionary trend: first, the specific surface area of Mn@EAC-0 (without manganese addition) after hyperaccumulation treatment is only 433.81 m$^2$ g$^{-1}$. With increasing manganese enrichment, the specific surface areas of Mn@EAC-10, Mn@EAC-20, and Mn@EAC-30 gradually increase to 516.37 m$^2$ g$^{-1}$, 619.82 m$^2$ g$^{-1}$, and the highest value of 635.24 m$^2$ g$^{-1}$, respectively. This trend positively correlates with the manganese content determined by ICP-OES, indicating that manganese species play an *in situ* pore-forming role during pyrolysis. However, when the enrichment time extends to 40 days (Mn@EAC-40), the specific surface area decreases to 489.74 m$^2$ g$^{-1}$, suggesting that excessive manganese may lead to pore blockage or structural collapse. Subsequently, the pore size distribution curve calculated using the BJH model (Fig. 2c) shows that Mn@EAC-30 exhibits a concentrated pore size distribution within the 2–5 nm range, with an average pore size of 3.36 nm. This size falls within the typical mesoporous range (2–50 nm) and is particularly conducive to the rapid diffusion and adsorption of hydrated Na$^+$ and Cl$^-$ ions.

Finally, the contact angle test demonstrated that the degree of manganese enrichment in the biomass char materials significantly affects the surface wetting properties of the composites. The experimental data show (see Fig. 2f and Fig. S3) that the contact angle of Mn@EAC-30 is significantly lower than those of other Mn@EAC-$x$ composites, indicating that the material has excellent hydrophilic properties. The enhancement of the surface wettability of the material contributes to
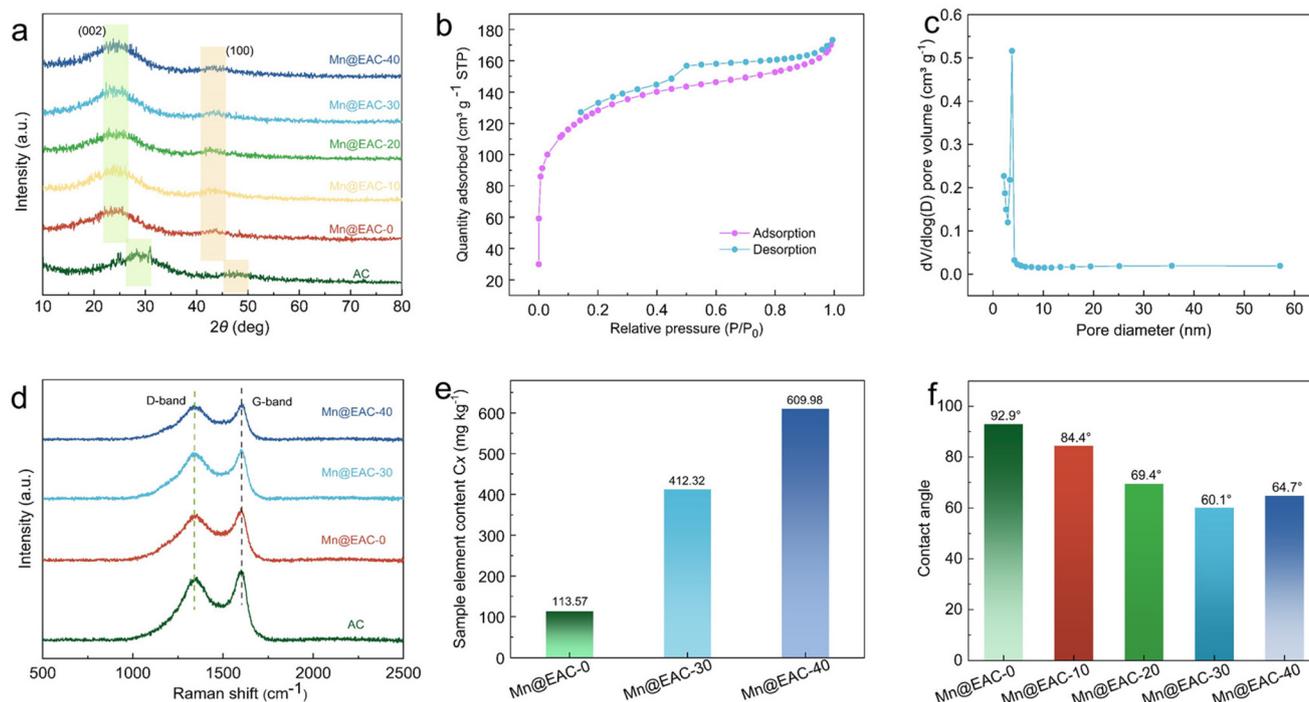
Fig. 2 Characterization of the physical properties of the materials. (a) X-ray diffraction (XRD) analysis of AC and Mn@EAC-*x*; (b and c) nitrogen adsorption−desorption isotherm and pore size distribution of Mn@EAC-30; (d) Raman spectroscopy analysis of AC and Mn@EAC-*x*; (e) inductively coupled plasma optical emission spectroscopy (ICP-OES) elemental content analysis of Mn@EAC-*x*; and (f) contact angle test of Mn@EAC-*x*.

the uniform dispersion of the self-doped manganese biomass-derived carbon material in the flowing electrode system, which in turn effectively inhibits the deposition of the electrode material in the delivery pipeline and the collector device, and thus improves its desalination performance.[36]

Fig. 3 and S4 present the scanning electron microscopy (SEM) images of AC and Mn@EAC-*x* composites with varying manganese doping levels. The AC sample (Fig. S4a) exhibits a typical activated carbon morphology, characterized by uneven pore distribution and disordered pore structures. In contrast, the Mn@EAC-*x* series (Fig. 3a and Fig. S4b–e) displays more abundant and well-organized hollow straight pore structures. The formation of such structures can be attributed to the preservation of the plant template's biological architecture during carbonization and the pore-forming effect induced by manganese species. With increasing manganese doping (from Mn@EAC-0 to Mn@EAC-40), the pore structures of the materials show a clear evolution trend: Mn@EAC-0 retains the microporous framework of the biomass precursor (Fig. S4b); Mn@EAC-10 and Mn@EAC-20 (Fig. S4c and d) show uniformly dispersed manganese oxide nanoparticles on the pore surfaces, which partially fill the original pores and promote the formation of new mesoporous structures; Mn@EAC-30 (Fig. 3a) exhibits the most optimized pore structure, with smooth pore walls and a uniformly distributed mesoporous structure, facilitating rapid electrolyte infiltration and ion transport. Notably, when the doping level further increases to Mn@EAC-40 (Fig. S4e), significant agglomeration of manga-

nese particles is observed, accompanied by partial collapse of the pore structure, which may explain the decrease in specific surface area and electrochemical performance.

Transmission electron microscopy (TEM) analysis further supports these findings. The TEM images of Mn@EAC-30 (Fig. 3b and c) reveal a typical amorphous porous structure, with no distinct lattice fringes observed in high-resolution images, indicating that the manganese species predominantly exist in an amorphous or nanocrystalline form. Selected area electron diffraction (SAED) patterns exhibit diffuse ring features (inset), further confirming the amorphous nature of the material. These morphological characteristics are highly consistent with the broad diffraction peaks in the XRD patterns and the high specific surface area (635.24 m² g⁻¹) and mesopore-dominated pore size distribution determined by BET measurements. Together, these results demonstrate that manganese doping effectively modulates the pore structure of biomass-derived carbon, providing a structural foundation for its excellent electrochemical performance and desalination capabilities. Immediately after that, the elemental distribution of the Mn@EAC-30 composite was characterized by EDS, as shown in Fig. 3d, and the test results indicated that the three elements C, O, and Mn showed a homogeneous distribution in the material.

### 3.2. Electrochemical properties

The electrochemical performance of AC and Mn@EAC-*x* was evaluated using a three-electrode system in 1 M NaCl solution
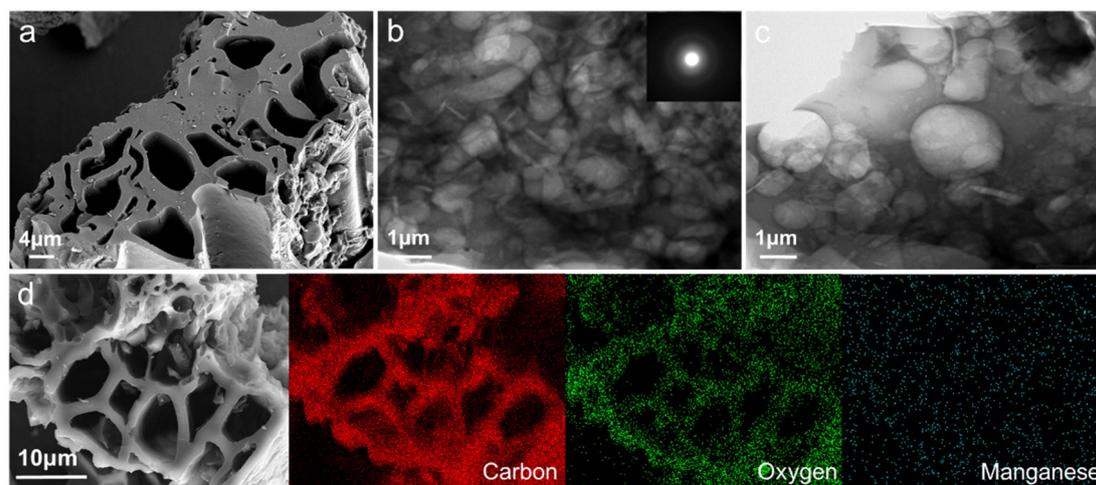
**Fig. 3** Morphological analysis of the Mn@EAC-30 material. (a) Scanning Electron Microscopy (SEM) image; (b and c) transmission electron microscopy (TEM) images; and (d) energy dispersive spectroscopy (EDS) elemental mapping image.

(as shown in Fig. 4 and S5). Fig. 4a shows the CV curves of Mn@EAC-30 at different scan rates from 5 to 50 mV s$^{-1}$. It is observed that all the CV curves show a symmetric quasi-rectangular morphology as the scan rate is increased, which suggests a typical bilayer capacitance property. Subsequently, GCD tests were performed on the Mn@EAC-30 material, as shown in Fig. 4b and Table S2, and their charge/discharge curves showed a symmetric morphology of approximate triangles, confirming that the electrode material possesses excel-

lent charge transport properties with good electrochemical reversibility. The calculated specific capacitances of materials AC, Mn@EAC-0, Mn@EAC-10, Mn@EAC-20, and Mn@EAC-30 at a current density of 0.25 A g$^{-1}$ are 176.03 F g$^{-1}$, 120.91 F g$^{-1}$, 90.23 F g$^{-1}$, 106.38 F g$^{-1}$, and 137.30 F g$^{-1}$, respectively. Furthermore, the electrochemical behaviour of AC and Mn@EAC-$x$ was investigated by cyclic voltammetry at a scan rate of 5 mV s$^{-1}$. As shown in Fig. 4c, the area enclosed by the CV curves tends to increase with the increase of the doped Mn
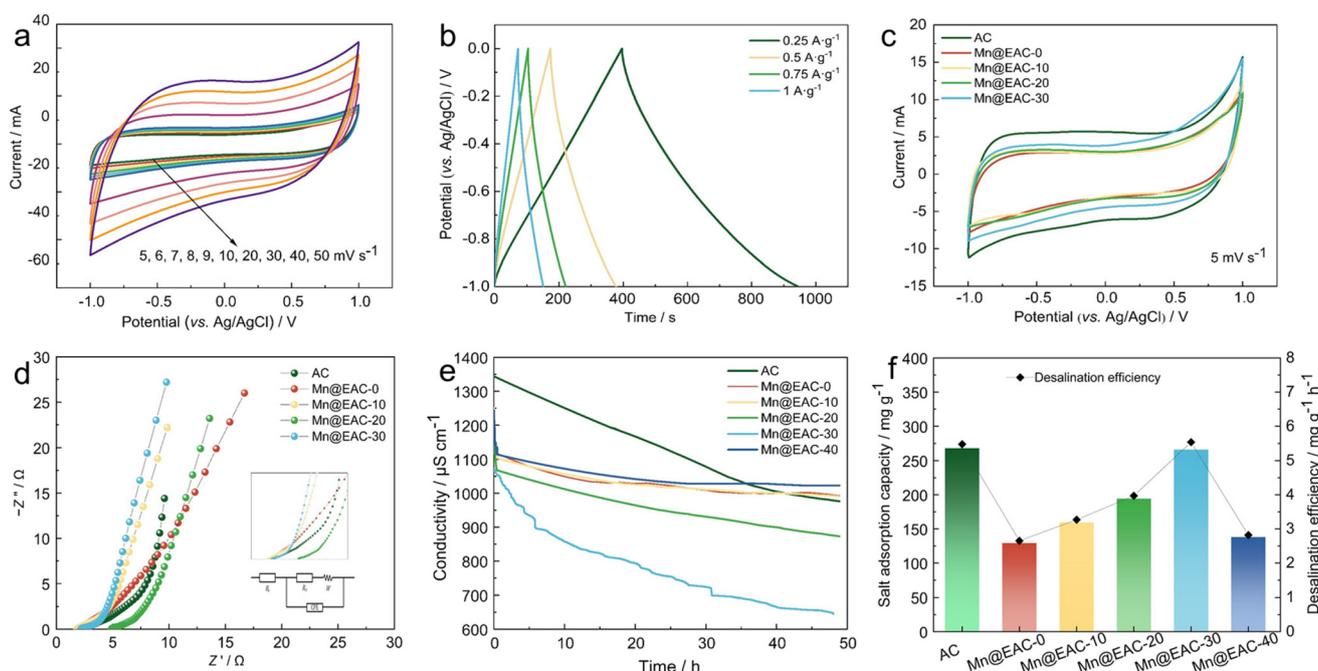


**Fig. 4** Electrochemical performance and desalination performance testing of the materials. (a) Cyclic voltammetry (CV) curves of Mn@EAC-30 at different scan rates; (b) galvanostatic charge−discharge (GCD) curves of Mn@EAC-30 at different current densities; (c) CV curves of AC and Mn@EAC-$x$ at a scan rate of 5 mV s$^{-1}$; (d) electrochemical impedance spectroscopy (EIS) curves of AC and Mn@EAC-$x$; and (e and f) desalination efficiency of AC and Mn@EAC-$x$.

content. This phenomenon is mainly attributed to the enrichment effect of EA on manganese and the synergistic effect between the biomass-derived carbon material and the doped manganese, which work together to significantly improve the electrochemical performance of Mn@EAC-$x$. Finally, in order to deeply investigate the kinetic characteristics of the self-doped manganese biomass-derived carbon material,[37] we performed EIS tests, and the results are displayed in Fig. 4d. Compared with the commercial AC material, the prepared Mn@EAC-$x$ material showed a significant decrease in the charge transfer resistance and a reduction in the ion diffusion internal resistance, suggesting that the material is a promising electrode material for FCDI.

According to the previous characterization and electrochemical tests, with the increase of manganese doping in biomass-derived carbon materials, the specific surface area and specific capacitance of the composites are significantly increased, and the charge impedance is also significantly reduced. Here, AC is used for comparison at an operating voltage of 1.0 V, an AC/Mn@EAC-$x$ content of 80 mg, and an electrode flow rate of 15 ml min$^{-1}$. The desalination properties of Mn@EAC-$x$ materials obtained under different cultivation period conditions were investigated. According to the experimental data in Fig. 4e and f, with the increase of manganese doping, the desalination capacity of the obtained Mn@EAC-$x$ gradually increases, and its performance reaches the best level at 30 days, and its salt adsorption capacity and average desalination rate reach 266.58 mg g$^{-1}$ and 5.55 mg g$^{-1}$ h$^{-1}$, respectively.

However, with further increase in manganese doping, the performance decreases sharply, which may be attributed to the synergistic effect of pore blockage and specific surface area attenuation induced by excessive manganese doping. Analysis of the existing characterization data reveals that although Mn@EAC-40 possesses the highest manganese content (609.98 mg kg$^{-1}$), its specific surface area (489.74 m$^2$ g$^{-1}$) is significantly lower than that of Mn@EAC-30. This seemingly paradoxical phenomenon precisely reveals the internal mechanism of performance degradation – excessive manganese species may form larger-sized clusters during the carbonization process. These clusters not only fail to effectively contribute active sites but also block the crucial mesoporous channels, thereby directly reducing the specific surface area available for ion adsorption, significantly increasing the ion diffusion resistance within the channels, and hindering adequate contact between the electrolyte and internal active sites. Therefore, when manganese doping exceeds the optimal level (30 days), the combined effects of mass transfer limitations caused by pore blockage and specific surface area attenuation outweigh the benefits, ultimately leading to the sharp decline in performance. Thus, the Mn@EAC-30 prepared from EA with a culture time of 30 days was selected for subsequent research.

### 3.3. Desalination performance

To investigate the desalination performance of the Mn@EAC-30 electrode in the FCDI system, we carried out desalination experiments under different electrode contents, working voltages, electrode flow rates and salt solution concentrations, and analyzed the difference of seawater desalination performances. Firstly, the effects of different electrode contents on the desalination performance of the FCDI system were discussed. As shown in Fig. 5a and b, with the increase of electrode content, the conductivity of the Mn@EAC-30 electrode material decreases continuously in a constant time, but its salt adsorption capacity and average desalination rate increase first and then decrease. This is because the density of active adsorption sites in the system increases with the increase of electrode content, the collision between active material particles is more frequent, and electrons can move more easily between particles, so the desalination performance will be better. However, when the electrode content is excessively high, its viscosity will increase accordingly, which will lead to the partial deposition of the active material in the hose and current collector, which will reduce the mobility of the ions and limit the transfer of charge, and is not conducive to the regeneration of the electrode material. Therefore, the system exhibited optimal desalination performance when the electrode loading reached 80 mg, specifically demonstrated by a salt adsorption capacity of up to 266.58 mg g$^{-1}$, with an average desalination rate stabilizing at 5.55 mg g$^{-1}$ h$^{-1}$.

Secondly, the working potential is a key parameter for the formation of the EDL and an important parameter affecting the operation of FCDI. Therefore, this study systematically examined the variations in the desalination performance of the FCDI system under different operating potential conditions. As shown in Fig. 5c and d, with the increase of the working voltage, the conductivity of simulated seawater decreases significantly, and the driving force of the ion migration of the Mn@EAC-30 flow electrode also increases. As the operating voltage increased from 0.8 V to 1.2 V, the salt adsorption capacity and average desalination rate of the Mn@EAC-30 flow electrode exhibited a significant linear growth trend. However, when the voltage continues to increase to 1.3 V, the upward trend of the desalination performance of the FCDI system is significantly reduced. At the same time, the increase of the input power of the FCDI system will inevitably lead to an increase in energy consumption. Therefore, it is not wise to continue to increase the working potential in order to improve the desalination efficiency. Therefore, 1.2 V is selected as the appropriate voltage for subsequent experiments.

It is well known that the degree of turbulence of the flow electrode is closely related to its flow velocity. Increasing the relative motion between particles can improve the stability of the conductive network. As depicted in Fig. 5e and f, the experimental findings demonstrate that the electrode flow rate exerts a considerable influence on the seawater desalination efficacy of Mn@EAC-30. When the electrode flow rate is increased to 25 mL min$^{-1}$, the system desalination performance reaches its optimal value, at which point the salt adsorption capacity reaches 357.08 mg g$^{-1}$ and the average desalination rate increases to 7.38 mg g$^{-1}$ h$^{-1}$. This is because within a certain range, the increase of the current flow rate can reduce
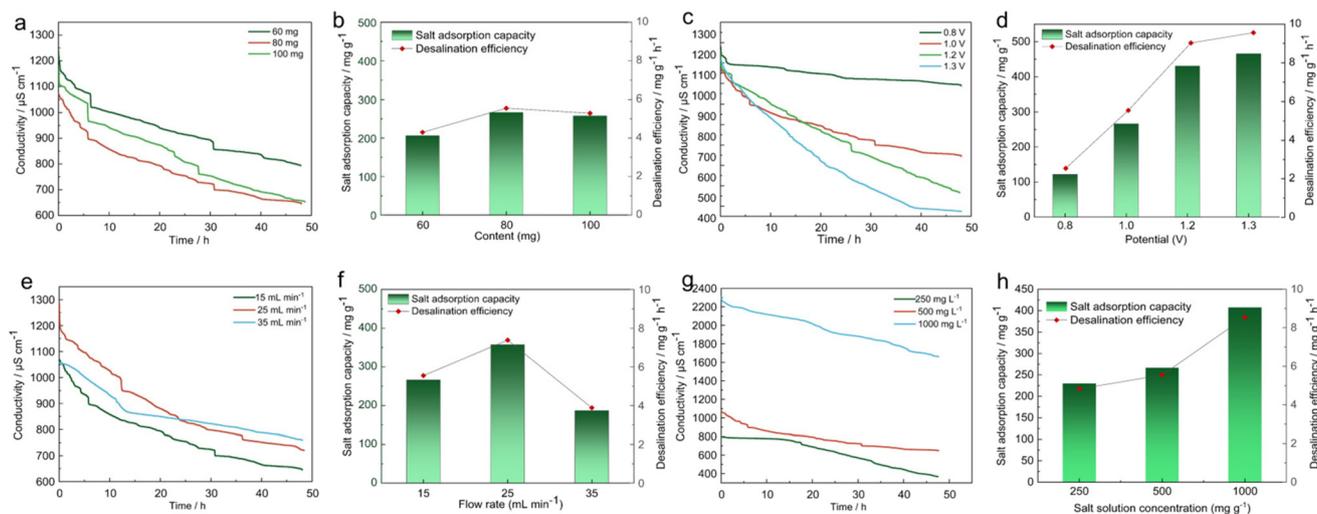
**Fig. 5** The FCDI desalination performance of Mn@EAC-30 in a 500 mg L$^{-1}$ NaCl solution. (a and b) The impact of varying electrode solid contents on desalination efficiency with an applied electrode potential of 1.0 V, an electrode flow rate of 15 mL min$^{-1}$ and a salt solution concentration of 500 mg L$^{-1}$; (c and d) the influence of different applied voltages on desalination performance with the flowing electrode solid content of 80 mg, an electrode flow rate of 15 mL min$^{-1}$ and a salt solution concentration of 500 mg L$^{-1}$; (e and f) the effect of varying electrode flow rates on the desalination process with the flowing electrode solid content of 80 mg, an applied electrode potential of 1.0 V, and the salt solution concentration of 500 mg L$^{-1}$. (g and h) The effect of salt solution concentration on the desalination process with the flowing electrode solid content of 80 mg, an applied electrode potential of 1.0 V, and an electrode flow rate of 15 mL min$^{-1}$.

the transfer resistance between electrons, thereby promoting the charge transfer rate between electrode particles and within the electrode flow channels, and ultimately enhancing the desalination efficiency of the FCDI system. When the electrode flow rate continues to increase, the diffusion path of ions in the solution is extended accordingly. Meanwhile, the wear effect of the high flow rate on the peristaltic pump and the ion exchange membrane cannot be ignored. So it will have a greater impact on the seawater desalination performance of the FCDI system.

Finally, to systematically evaluate the applicability of the Mn@EAC-30 electrode in actual water bodies, this study investigated the effect of salt solution concentration on its FCDI desalination performance. As shown in Fig. 5g, as the NaCl solution concentration increased from 250 mg L$^{-1}$ to 1000 mg L$^{-1}$, the system conductivity exhibited a stepwise decline, with a more pronounced rate of decrease in the higher concentration range, indicating enhanced ion migration driving force at elevated salinity levels. The results in Fig. 5h demonstrate that both the salt adsorption capacity and average desalination rate of Mn@EAC-30 significantly improved with increasing influent salt concentration. Specifically, at 250 mg L$^{-1}$, the salt adsorption capacity was 230 mg g$^{-1}$, and the average desalination rate was 4.83 mg g$^{-1}$ h$^{-1}$; when the concentration was raised to 500 mg L$^{-1}$, the salt adsorption capacity increased to 266.58 mg g$^{-1}$, with a desalination rate of 5.55 mg g$^{-1}$ h$^{-1}$; and at a further elevated concentration of 1000 mg L$^{-1}$, the salt adsorption capacity reached 407.5 mg g$^{-1}$, accompanied by a desalination rate of 8.55 mg g$^{-1}$ h$^{-1}$. This trend aligns with electric double-layer theory and ion transport kinetics: higher ion concentrations provide stronger electrochemical

driving forces, promoting the formation of electric double layers on the electrode surface and enhancing ion adsorption, thereby improving desalination efficiency. These findings indicate that the Mn@EAC-30 electrode exhibits favorable concentration adaptability across a relatively broad salinity range (250–1000 mg L$^{-1}$), particularly suited for desalination treatment of medium-to-high salinity water bodies, providing experimental support for its practical applications in seawater desalination and high-salinity wastewater reuse.

Additionally, this study systematically investigated the stability performance of the Mn@EAC-30 flow electrode during long-term continuous cycling in an FCDI system. The specific experimental conditions were as follows: a NaCl solution concentration of 500 mg L$^{-1}$, an operating voltage of 1.2 V, an electrode flow rate of 25 mL min$^{-1}$, and a Mn@EAC-30 solid content in the flow electrode of 80 mg. In Fig. 6, the Mn@EAC-30 flow electrode shows good operational consistency over five consecutive desalination cycles, with both its salt adsorption capacity and average desalination rate maintained at approximately 70% of their initial values.

It is noteworthy that the desalination performance of the material still experienced a certain degree of decay during the cycling process. To elucidate the mechanism behind this performance decline, scanning electron microscopy (SEM) and contact angle tests were conducted on the cycled material (results shown in Fig. S6). SEM images revealed that the overall morphology of the material remained intact, but evident particle agglomeration was observed within its hollow straight channels. Simultaneously, the surface wettability of the material significantly weakened, with the contact angle increasing from 60.1° before cycling to 75.9° after cycling. The
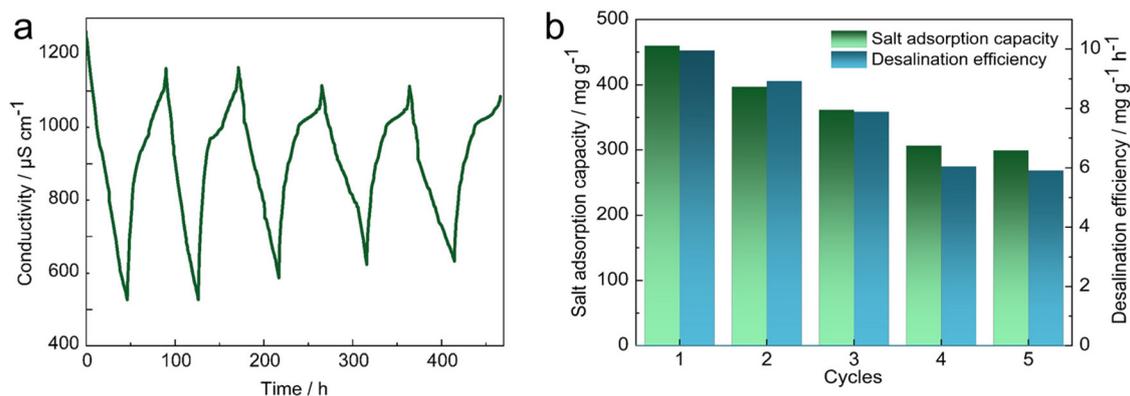
**Fig. 6** Desalination cycling performance of the Mn@EAC-30 electrode in a 500 mg L$^{-1}$ NaCl solution, with an applied electrode potential of 1.2 V and an electrode flow rate of 25 mL min$^{-1}$: (a) the graph shows the variation in conductivity over the cycle time. (b) The salt adsorption capacity and the average desalination performance of the material are depicted for different cycle counts.

decline in surface hydrophilicity, along with the agglomeration of active materials, may collectively lead to reduced dispersion uniformity of the electrode slurry, exacerbate local concentration polarization, and increase the ion transport resistance at the electrode/electrolyte interface. These factors work together to contribute to the gradual attenuation of desalination performance.

The above results indicate that although the Mn@EAC-30 electrode material exhibits good structural retention and performance stability during cycling, the evolution of its interfacial properties remains a key factor influencing long-term operational efficiency.[38,39] This study provides important insights into understanding the degradation behavior of flow electrodes in FCDI systems and points the way for further optimization of material interface design to enhance long-term desalination stability.

In short, as shown in Fig. 7, a novel and green preparation method was adopted in this work, which first used the super-accumulation characteristics of EA to super-enrich metal

manganese ions from wastewater, and then carbonized to prepare self-doped manganese biomass-derived carbon materials for FCDI seawater desalination treatment, showing excellent performance.

## 4. Conclusion

Self-doped manganese biomass-derived porous carbon composites were successfully prepared by a green and simple superaccumulation and carbonization. The transition metal manganese elements were uniformly distributed on the biomass-derived carbon materials by the bioabsorption method using EA, and the synergistic effect between the electric double-layer capacitance of the biomass-derived carbon matrix and the pseudocapacitance of the transition metal manganese was used to make the Mn@EAC-30 material a porous material with a high specific surface area of 635.24 m$^2$ g$^{-1}$ and a specific capacitance of 137.39 F g$^{-1}$ at a current density of 0.25 A g$^{-1}$. The salt adsorption capacity and average desalination retention rate of the FCDI system assembled with this material were about 70% after long-term desalination cycles. This work provides a simple, controllable and eco-friendly method for the synthesis of transition metal element self-doped biomass-derived porous carbons as advanced electrode materials for FCDI desalination application.

## Conflicts of interest

There are no coflicts to declare.

## Data availability

Data will be made available upon request.
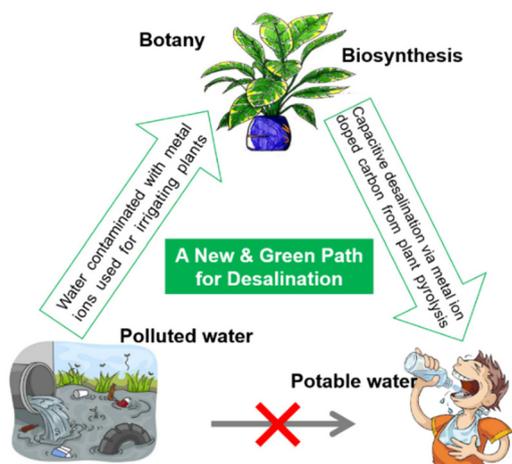
Supplementary information (SI) is available. See DOI: https://doi.org/10.1039/d5nr04506a.



**Fig. 7** A new and green biosynthesis path for desalination application.

# Acknowledgements

# References

1 B. Fu, X. Zhang, N. Robinson, Z. Zhang, J. Zhang, J. Ji, Y. Xu, K. Zhang, M. Dong, J. Kang, L. Zhang, L. Wang, Y. Zou, M. Zhou, S. Chen, H. Yin, H. Xu, P. Liu and H. Zhao, Multi-shelled hollow porous carbon nanospheres-based evaporator for highly efficient solar-driven desalination, *Nano Energy*, 2024, **129**, 110054, DOI: 10.1016/j.nanoen.2024.110054.

2 O. Shamet and M. Antar, Mechanical vapor compression desalination technology – A review, *Renewable Sustainable Energy Rev.*, 2023, **187**, 113757, DOI: 10.1016/j.rser.2023.113757.

3 Z. Wang, Y. Zhang, T. Wang, B. Zhang and H. Ma, Design and energy consumption analysis of small reverse osmosis seawater desalination equipment, *Energies*, 2021, **14**(8), 2275, DOI: 10.3390/en14082275.

4 G. Doornbusch, M. van der Wal, M. Tedesco, J. Post, K. Nijmeijer and Z. Borneman, Multistage electrodialysis for desalination of natural seawater, *Desalination*, 2021, **505**, 114973, DOI: 10.1016/j.desal.2021.114973.

5 Z.-Q. Yang, W.-B. Zhang, K. Yang, B. Chen, Y. Yin, J.-J. Li, J.-L. Yang, Y. Gao and X.-J. Ma, Switchable NaCl cages via a MWCNTs/Ni[Fe(CN)6]2 nanocomposite for high performance desalination, *Nanoscale*, 2023, **15**(47), 19330–19338, DOI: 10.1039/D3NR04410F.

6 S. Dahiya, A. Singh and B. K. Mishra, Capacitive deionized hybrid systems for wastewater treatment and desalination: A review on synergistic effects, mechanisms and challenges, *Chem. Eng. J.*, 2021, **417**, 128129, DOI: 10.1016/j.cej.2020.128129.

7 T. Alencherry, A. R. Naveen, S. Ghosh, J. Daniel and R. Venkataraghavan, Effect of increasing electrical conductivity and hydrophilicity on the electrosorption capacity of activated carbon electrodes for capacitive deionization, *Desalination*, 2017, **415**, 14–19, DOI: 10.1016/j.desal.2017.04.001.

8 S.-I. Jeon, H.-R. Park, J.-G. Yeo, S. Yang, C. H. Cho, M. H. Han and D. K. Kim, Desalination via a new membrane capacitive deionization process utilizing flow-electrodes, *Energy Environ. Sci.*, 2013, **6**(5), 1471–1475, DOI: 10.1039/C3EE24443A.

9 F. Yu, Z. Yang, Y. Cheng, S. Xing, Y. Wang and J. Ma, A comprehensive review on flow-electrode capacitive deionization: Design, active material and environmental application, *Sep. Purif. Technol.*, 2022, **281**, 119870, DOI: 10.1016/j.seppur.2021.119870.

10 Z. Li, B. Li, L. Du, W. Wang, X. Liao, H. Yu, C. Yu, H. Wang and Q. Li, Three-dimensional oxygen-doped porous graphene: Sodium chloride-template preparation, structural characterization and supercapacitor performances,

*Chin. J. Chem. Eng.*, 2021, **40**, 304–314, DOI: 10.1016/j.cjche.2020.11.042.

11 Z. Xie, X. Shang, J. Yan, T. Hussain, P. Nie and J. Liu, Biomass-derived porous carbon anode for high-performance capacitive deionization, *Electrochim. Acta*, 2018, **290**, 666–675, DOI: 10.1016/j.electacta.2018.09.104.

12 H. Xu, S. Zhong, C. Yuan, X. Zheng and S. Wang, Honeycomb-like N, S dual-doped porous carbons derived from pomelo peel by effective exogenous doping strategy for supercapacitor electrodes, *Diamond Relat. Mater.*, 2024, **150**, 111768, DOI: 10.1016/j.diamond.2024.111768.

13 S. Zhong, L. Dai, H. Xu, X.-C. Yang, X. Zheng and S. Wang, Highly porous carbon with selective transformation of nitrogen groups boosts the capacitive performance through boric acid template assisted strategy, *J. Energy Storage*, 2024, **97**, 112867, DOI: 10.1016/j.est.2024.112867.

14 S. Liu, X. Chen, X. Li, P. Huo, Y. Wang, L. Bai, W. Zhang, M. Niu and Z. Li, Nitrogen- and oxygen-containing micro-mesoporous carbon microspheres derived from m-aminophenol formaldehyde resin for supercapacitors with high rate performance, *RSC Adv.*, 2016, **6**(92), 89744–89756, DOI: 10.1039/c6ra16608c.

15 J. Cheng, S.-C. Hu, G.-T. Sun, K. Kang, M.-Q. Zhu and Z.-C. Geng, Comparison of activated carbons prepared by one-step and two-step chemical activation process based on cotton stalk for supercapacitors application, *Energy*, 2021, **215**, 119144, DOI: 10.1016/j.energy.2020.119144.

16 M. M. Sk, P. Pradhan, B. K. Patra and A. K. Guria, Green biomass derived porous carbon materials for electrical double-layer capacitors (EDLCs), *Mater. Today Chem.*, 2023, **30**, 101582, DOI: 10.1016/j.mtchem.2023.101582.

17 R. B. Marichi, S. Goel, A. K. Tomar, V. Sahu, S. Lalwani, G. Singh and R. K. Sharma, Direct hydrothermal treatment of sugarcane juice for 3D oxygen-rich carbon Aerogel/NiCo2O4 based supercapacitor, *Mater. Chem. Phys.*, 2020, **239**, 121957, DOI: 10.1016/j.matchemphys.2019.121957.

18 Y. Zhang, C.-R. Chang, X.-D. Jia, Q.-Y. Huo, H.-L. Gao, J. Yan, A.-Q. Zhang, Y. Ru, H.-X. Mei, K.-Z. Gao and L.-Z. Wang, Morphology-dependent NiMoO4/carbon composites for high performance supercapacitors, *Inorg. Chem. Commun.*, 2020, **111**, 107631, DOI: 10.1016/j.inoche.2019.107631.

19 H. Wang, H. Chen, X. Hou, H. Ye, Z. Guo, Z. Chen, Y. Jin, Y. Du and P. Ren, MnO decorated biomass derived carbon based on hyperaccumulative characteristics as advanced electrode materials for high-performance supercapacitors, *Diamond Relat. Mater.*, 2023, **136**, 109888, DOI: 10.1016/j.diamond.2023.109888.

20 W. Xu, L. Liu and W. Weng, High-performance supercapacitor based on MnO/carbon nanofiber composite in extended potential windows, *Electrochim. Acta*, 2021, **370**, 137713, DOI: 10.1016/j.electacta.2021.137713.

21 W. Xu, L. Liu and W. Weng, High-performance supercapacitor based on MnO/carbon nanofiber composite in extended potential windows, *Electrochim. Acta*, 2021, **370**, 137713, DOI: 10.1016/j.electacta.2021.137713.

22 D. Van Lam, U. N. T. Nguyen, E. Roh, W. Choi, J.-H. Kim, H. Kim and S.-M. Lee, Graphitic Carbon with MnO/Mn$_7$C$_3$ Prepared by Laser-Scribing of MOF for Versatile Supercapacitor Electrodes, *Small*, 2021, **17**(29), 2100670, DOI: 10.1002/smll.202100670.

23 D. Han, Y. Shen, Y. Zhao, Y. Pan, J. Wei and Y. Wei, Porously nanostructured MnO/C composites directed from polydopamine as high-performance supercapacitor electrodes, *J. Mater. Sci.: Mater. Electron.*, 2021, **32**(5), 5781–5789, DOI: 10.1007/s10854-021-05298-7.

24 H. Li, H. Yang, H. Sun, Y. Huang, P. An, Y. Yunhua and H. Zhao, A manganese oxide/biomass porous carbon composite for high-performance supercapacitor electrodes, *Electrochim. Acta*, 2024, **473**, 143514, DOI: 10.1016/j.electacta.2023.143514.

25 X. Zhao, N. Wang, L. Li, Z. Fang, S. Tang and J. Gu, Sea Urchin-Like MnO$_2$/Biomass Carbon Composite Electrode Material for High-Performance Supercapacitors, *J. Chem.*, 2024, **2024**, 11, DOI: 10.1155/2024/2779104.

26 H. Ahmadi, *Functional Analysis of the Metal Hyperaccumulation and Hypertolerance Candidate Genes NAS4, ZIP6, CAX1 and NRAMP3 in Arabidopsis halleri*, ProQuest LLC, 2017.

27 N. T. Dinh, D. T. Vu, D. Mulligan and A. V. Nguyen, Accumulation and distribution of zinc in the leaves and roots of the hyperaccumulator Noccaea caerulescens, *Environ. Exp. Bot.*, 2015, **110**, 85–95, DOI: 10.1016/j.envexpbot.2014.10.001.

28 I. Sánchez-Castro, L. Molina, M.-Á. Prieto-Fernández and A. Segura, Past, present and future trends in the remediation of heavy-metal contaminated soil - Remediation techniques applied in real soil-contamination events, *Heliyon*, 2023, **9**(6), e16692, DOI: 10.1016/j.heliyon.2023.e16692.

29 J. Hua, C. Zhang, Y. Yin, R. Chen and X. Wang, Phytoremediation potential of three aquatic macrophytes in manganese-contaminated water, *Water Environ. J.*, 2012, **26**(3), 335–342, DOI: 10.1111/j.1747-6593.2011.00293.x.

30 O. E. Nworie, J. Qin and C. Lin, Trace Element Uptake by Herbaceous Plants from the Soils at a Multiple Trace Element-Contaminated Site, *Toxics*, 2019, **7**(3), DOI: 10.3390/Toxics7010003.

31 J. Zhou, Z.-Q. Yang, Y. Kang, X.-Y. Yuan, J. Feng, J.-H. Liu, X.-J. Ma and W.-B. Zhang, Carbonaceous C@FeS Flow Electrode for Electrochemical Capacitive Deionization Application, *J. Electrochem. Soc.*, 2024, **171**, 114509, DOI: 10.1149/1945-7111/ad85fb.

32 Z.-Q. Yang, W.-B. Zhang, S.-B. Guo, M. M. Theint, Y. Yin, J.-J. Li, J.-L. Yang and X.-J. Ma, Flow Electrode Capacitive Deionization System with Simultaneous Desalting of Na$^+$ and Gathering of Na$^+$, *Langmuir*, 2022, **38**(50), 15740–15746, DOI: 10.1021/acs.langmuir.2c02628.

33 T. Wang, Y. Sun, L. Zhang, K. Li, Y. Yi, S. Song, M. Li, Z.-A. Qiao and S. Dai, Space-Confined Polymerization: Controlled Fabrication of Nitrogen-Doped Polymer and Carbon Microspheres with Refined Hierarchical Architectures, *Adv. Mater.*, 2019, **31**(16), 1807876, DOI: 10.1002/adma.201807876.

34 Y. Lian, Y. Zheng, Z. Wang, Y. Hu, J. Zhao and H. Zhang, Multidefect N-Nb$_2$O$_5$-$x$@CNTs Incorporated into Capillary Transport Framework for Li$^+$/Na$^+$ Storage, *Small*, 2022, **18**(23), 2201450, DOI: 10.1002/smll.202201450.

35 S. Liu, S. Wu, H. Cheng, W. Wei and F. Zhang, Sodium lignosulfonate derived hierarchical porous carbon spheres for VOC removal and supercapacitors, *Ind. Crops Prod.*, 2022, **179**, 114657, DOI: 10.1016/j.indcrop.2022.114657.

36 J. Ma, C. Zhai and F. Yu, Review of flow electrode capacitive deionization technology: Research progress and future challenges, *Desalination*, 2023, **564**, 116701, DOI: 10.1016/j.desal.2023.116701.

37 S. Liu, Q. Wang, B. Li, Y. Zhou, T. Gong and J. Li, Preparation of nitrogen-doped hierarchical porous carbon electrodes for high performance capacitive deionization, *Ionics*, 2023, **29**(7), 2935–2945, DOI: 10.1007/s11581-023-05051-6.

38 S. Guo, Y. Zhang, Z. Yu, M. Dai, X. Liu, H. Wang, S. Liu, J. Justin Koh, W. Sun, Y. Feng, Y. Chen, L. Yang, P. Sun, G. Lu, C. Yu, W. Chen, S. De Wolf, Z. Wang and S. C. Tan, Leaf-based energy harvesting and storage utilizing hygroscopic iron hydrogel for continuous power generation, *Nat. Commun.*, 2025, **16**(1), 5267, DOI: 10.1038/s41467-025-60341-z.

39 S. Guo, S. Zhang, H. Li, S. Liu, J. J. Koh, M. Zhou, Z. Sun, Y. Liu, H. Qu, Z. Yu, Y. Zhang, L. Yang, W. Chen, C. He, C. Lee, D. Mao, S. K. Ravi, Y. Lai and S. C. Tan, Precisely manipulating polymer chain interactions for multifunctional hydrogels, *Matter*, 2025, **8**(4), 101785, DOI: 10.1016/j.matt.2024.06.024.